3B.3   Wind-shear Detection Performance Analysis for MPAR Risk Reduction

John Y. N. Cho, Robert S. Frankel, Michael F. Donovan, Mark S. Veillette
MIT Lincoln Laboratory, Lexington, Massachusetts

Pamela L. Heinselman
NOAA National Severe Storms Laboratory, Norman, Oklahoma

Abstract - Multifunction phased array radars (MPARs) of the future that may replace the current terminal wind-shear detection systems will need to meet the Federal Aviation Administration's (FAA) detection requirements. Detection performance issues related to on-airport siting of MPAR, its broader antenna beamwidth relative to the Terminal Doppler Weather Radar (TDWR), and the change in operational frequency from C band to S band are analyzed. Results from the 2012 MPAR Wind-Shear Experiment are presented, with microburst and gust-front detection statistics for the Oklahoma City TDWR and the National Weather Radar Testbed (NWRT) phased array radar, which are located 6 km apart. The NWRT has sensitivity and beamwidth similar to a conceptual terminal MPAR (TMPAR), which is a scaled-down version of a full-size MPAR. The micro-burst results show both the TDWR probability of detection (POD) and the estimated NWRT POD exceeding the 90% requirement. For gust fronts, however, the overall estimated NWRT POD was more than 10% lower than the TDWR POD. NWRT data are also used to demonstrate that rapid-scan phased array radar has the potential to enhance microburst prediction capability.

1. INTRODUCTION

As the current radars that perform weather and aircraft surveillance over the United States age, they must be sustained through service life extension programs or be replaced. In the latter case, the radars can be replaced by multiple types of radars with different missions or they can be replaced by scalable MPARs (Weber et al., 2007; Benner et al., 2009). MPARs would operate in the band currently occupied by the Airport Surveillance Radars (ASRs) and Next Generation Weather Radar (NEXRAD), and be able to accomplish all of the missions conducted by the current multiplicity of radars with just one type of radar scaled to two variants—a full-size MPAR capable of aircraft and weather surveillance for both terminal and en route missions, and a scaled down TMPAR responsible for only terminal surveillance (Figure 1).

_____

Corresponding author address: John Y. N. Cho, MIT Lincoln Laboratory, 244 Wood St., S1-539F, Lexington, MA 02420-9185; e-mail: jync@ll.mit.edu.

State-of-the-art active phased array systems have the potential to provide improved capabilities such as earlier detection and better characterization of hazardous weather phenomena, 3D tracking of non-cooperative aircraft, better avoidance of unwanted clutter sources such as wind farms, and more graceful performance degradation with component failure. Because of the overlap in coverage provided by the current radar networks, a unified MPAR replacement network can potentially decrease the total number of radars needed to cover the same airspace (Cho et al., 2012), thus leading to cost savings as well. As the U.S. aviation community works toward realizing the Next Generation Air Transportation System (NextGen), achieving improved capabilities for aircraft and weather surveillance becomes critical, because stricter observation requirements are believed to be needed (Souders et al., 2010). Hence, the FAA is considering the MPAR as a possible solution to their NextGen Surveillance and Weather Radar Capability (NSWRC).
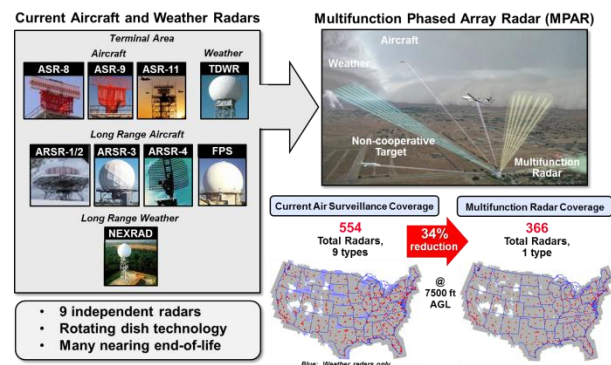

Figure 1.   Illustration of the MPAR concept.

There are risks associated in developing the MPAR system. Cost is obviously a concern, as phased array radars have traditionally been very expensive to procure. Since the minimum beamwidth requirement drives the antenna size, which, in turn, directly impacts the radar cost, we need to be judicious in our approach to beamwidth specification. Initial analysis has indicated that requiring the MPAR to match the 0.55° beamwidth of the TDWR (Michelson et al., 1990), one of the radars that would be replaced by MPAR, would likely result in unacceptably high cost. However, since the TDWR performs a safety-critical function—detecting hazardous wind shear near airports—we need to demonstrate that any relaxation of system specifications would still result in acceptable mission performance.

Ideally, an MPAR prototype would be used in the

demonstration of wind-shear detection performance. Being still a number of years away from a prototype, we opted to use the NWRT (Zrnic et al., 2007; Forsyth et al., 2009) as a proxy for the scaled down TMPAR (Figure 2) in a wind-shear observation field experiment. This report will first discuss the wind-shear detection performance issues, describe the experiment, and then give the results of the performance assessment.

Current Terminal Wind Shear Radars			4-m antenna	8-m antenna
	ASR-9 WSP	TDWR	TMPAR	MPAR
Location	On airport	Off airport	On airport	On/off airport
Operational band	S band	C band	S band	S band
Sensitivity @ 20 km	0 dBZ	-19 dBZ	0 dBZ	-19 dBZ
Beamwidth (AZ x EL)	1.4° x 5°	0.55° x 0.55°	1.6° x 1.6°*	0.9° x 0.9°*
Dual polarization	No	No	Yes	Yes
Rapid adaptive 3D scan	No	No	Yes	Yes

*At broadside

Figure 2. Comparison of relevant characteristics between today's ground-based terminal wind-shear detection radars and MPAR. (Disclaimer: MPAR and TMPAR characteristics are only notional at this time. System specifications are still to be determined.)

2. MPAR WIND-SHEAR DETECTION ISSUES

Currently in the National Airspace System (NAS), there are three types of ground-based terminal wind-shear detection systems: (1) The Low Level Windshear Alert System (LLWAS), (2) the ASR-9 Weather Systems Processor (WSP), and (3) the TDWR. LLWAS (Wilson and Gramzow, 1991) is an anemometer-based wind field measurement system that has coverage limited to some fraction of an airport's Areas Noted for Attention (ARENA). The ARENA is defined as the union of one nautical mile (NM) squares centered and concatenated along each runway centerline, and extending three NM beyond the runway end points along the take-off and landing paths. The WSP is an add-on system to the ASR-9 that processes the radar data separately from the aircraft detection channel in a way that is optimized for wind-shear detection (Weber and Stone, 1995). Performance, however, is limited by the fact that the ASR-9's inherent characteristics and scanning scheme are optimized for rapid-update reports of 2D aircraft location, not fine resolution measurements of near-surface winds. The TDWR was specifically designed for low-altitude wind-shear detection, and therefore exhibits the best performance of the three systems for this purpose. The Weather Surveillance Radar-1988 Doppler (WSR-88D), more commonly known as NEXRAD (Heiss et al., 1990), is also capable of wind-shear detection, although only some of them are close enough to airports to be useful in this regard (Cho and Hallowell, 2008).

TDWR requirements (FAA, 1995) call for detection of hazardous wind shear from ground level to 1,500 ft up to 6-NM range from the airport reference point (ARP) (Figure 3). This is a safety-critical requirement. The TDWR is also required to detect gust fronts within 40 NM (74 km) of the ARP. This, on the other hand, is an operational efficiency requirement, since early detection of gust fronts headed toward the airport allows control-

lers to plan for runway changes in advance of the actual wind shift. A minimum wind-shear detection probability of 90% and maximum false alarm rate of 10% are specified (FAA, 1987), although in practice these requirements are applied only to microbursts in the ARENA (T. Weyrauch, private communication).

One of the key parameters in any radar-based terminal wind-shear detection scheme is the location of the radar relative to the airport. TDWRs are located 10 to 24 km from the ARP, whereas ASR-9 WSPs are located on the airport grounds. The advantages of off-airport location are (1) ease of viewing the full coverage volume over the airport without resorting to extremely high antenna elevation angles, (2) limitations in minimum observation range does not affect near-airport coverage, and (3) less ground clutter contamination over the airport region. The advantages of on-airport location are (1) radar sensitivity (power aperture product) can be reduced because the range to the required coverage area is shorter, (2) beamwidth specification can be relaxed since the range to the required coverage area is shorter, (3) wind measurements can be made closer to the ground near the airport, and (4) life cycle cost of the radar site may be reduced if a location outside of the airport does not have to be leased and maintained.
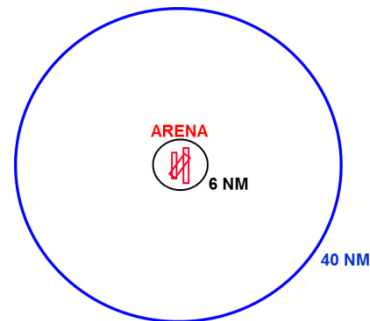

Figure 3. Illustration of TDWR wind-shear detection coverage regions. The ARP is at the center. The black circle indicates the required microburst detection coverage region and the blue circle outlines the required gust-front detection area.

In the MPAR siting study (Cho et al., 2012) we chose to put the TDWR-replacement MPARs on the airport, primarily because we wanted the aircraft surveillance coverage to extend down to the airport surface as the current ASR coverage does (Figure 4). This choice also allows us to relax the sensitivity and beamwidth requirements for MPAR.

How much can the sensitivity and beamwidth requirements be relaxed if MPAR is located on the airport? First, let us examine the sensitivity issue. In order to be able to detect microbursts, the radar must be sensitive enough to distinguish the outflow signature from the background noise or clutter. The distribution of microburst outflow reflectivity depends on the location (Figure 5). At a site where dry microbursts occur often (e.g., Denver), the minimum reflectivity that must be detected is much lower than at a location where only wet micro-

bursts occur (e.g., Orlando). However, reflectivity is not the only variable in determining detectability. Because microburst outflows and gust fronts are limited in vertical extent, less of the radar pulse volume gets filled at far range as the elevation beamwidth increases (Figure 6). Consequently, the effective sensitivity of the radar to these phenomena decreases with beamwidth faster than for normal volume-filling phenomena. Again, this is location dependent for microbursts, since the distribution of outflow depth varies with type (wet or dry) of microburst (Figure 7).
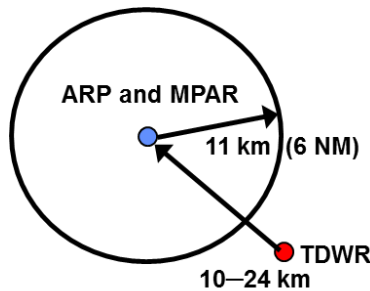

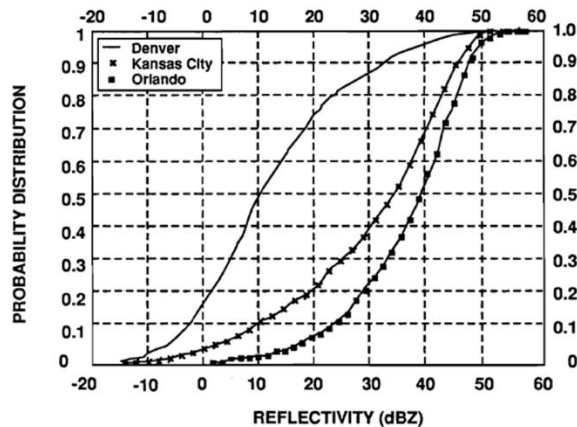Figure 4. Illustration of proposed MPAR location relative to current TDWR location.

Figure 5. Measured summer microburst outflow reflectivity cumulative density functions (CDFs) at the time of maximum shear (Biron and Isaminger, 1991).

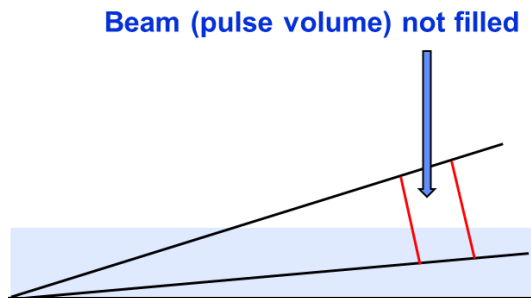**Beam (pulse volume) not filled**

Figure 6. Illustration of partial pulse volume filling by microburst outflow or gust front indicated by the light-blue layer.

Minimum detectable weather reflectivity (i.e., sensitivity) vs. range curves are plotted in Figure 8 for microburst

observation with the partial volume filling loss (Cho and Martin, 2007) factored in for a fixed outflow depth of 300 m. For a typical TDWR location of 18 km from the ARP, the required 11-km-radius coverage area for microbursts spans 7 to 29 km in range from the radar (green box in Figure 8). If MPAR and TMPAR are located at the airport, then the required coverage area is encompassed by the yellow box. The MPAR sensitivity limits within the yellow box are at least as good as the TDWR sensitivity limits in the green box, and both have enough sensitivity for dry and wet microbursts. However, the TMPAR, even with on-airport location, has significantly worse sensitivity in the yellow box than the TDWR in the green box. Its sensitivity is good enough for wet microbursts, but not for dry microbursts.
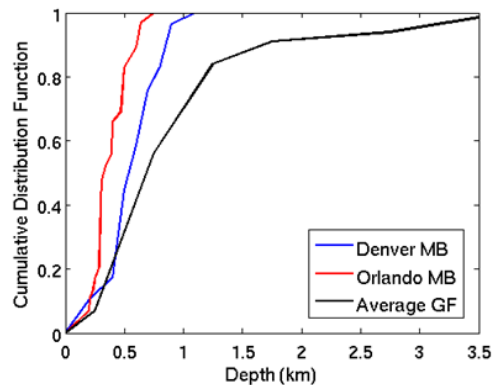

Figure 7. Measured depth CDFs of microburst (MB) outflows and gust fronts (GFs). Compiled from Wolfson et al. (1990), Biron and Isaminger (1991), and Weber et al. (1995).
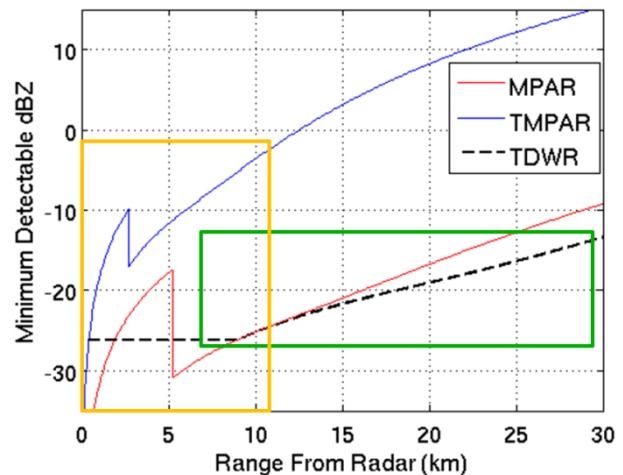

Figure 8. Minimum detectable reflectivity for microburst outflows plotted against range for TDWR and notional MPAR and TMPAR. Volume filling loss is included for a fixed outflow depth of 300 m. The discontinuities in the MPAR and TMPAR curves reflect the transition from short pulse to long pulse mode. The flattening of the TDWR curve at close range is due to the built-in sensitivity time control (STC) function.

Sensitivity plots for gust-front detection are shown in Figure 9. Although the original requirements called for

gust-front detection out to 40 NM (74 km) from the airport, the current TDWR product generator only outputs detections out to 60 km from the radar (FAA, 2004). Gust-front reflectivity statistics do not vary significantly with location, and the minimum reflectivity is about -5 dBZ (Klingle-Wilson and Donovan 1991). At far ranges the TMPAR can be expected to miss some fraction of gust fronts.
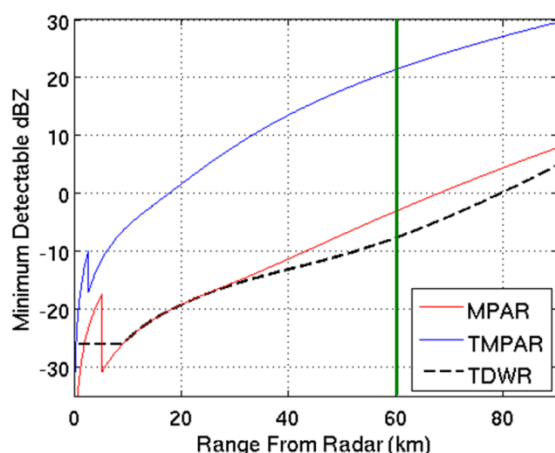

Figure 9. Minimum detectable reflectivity for gust fronts plotted against range for TDWR and notional MPAR and TMPAR. Volume filling loss is included for a fixed gust-front depth of 700 m. Currently, gust-front products are generated out to 60 km from the TDWR.

Microburst outflow velocity divergence decreases with height (Figure 10). Since the microburst detector relies on the magnitude of the divergence, the radar ideally observes the maximum velocity difference near the surface. The thickness of the antenna beam in the vertical dimension, however, can smear out the velocity measurement by effectively averaging the flows at different altitudes. For example, the vertical thickness of the TDWR antenna beam is 67 to 280 m within the critical 11-km radius around the airport for a TDWR located 18 km from the ARP. For an MPAR at the airport, the vertical beam thickness is 8 to 170 m within 11 km for a vertical beamwidth of 0.9° at 0° elevation. For a TMPAR, the thickness is 14 to 330 m for a vertical beamwidth of 1.7° at 0° elevation. (In our notional MPAR and TMPAR, the antenna faces are tilted 15° up in elevation, so the 0° elevation beam would be pointed 15° off broadside.) In this respect, therefore, the MPAR is expected to outperform the TDWR and the TMPAR should be comparable to the TDWR if they are located on the airport. If they are located off the airport at distances similar to the TDWR, then the MPAR and TMPAR would have more vertical smearing than the TDWR.

Azimuthal resolution is another concern if the beam-width requirements are relaxed. However, because the TDWR antenna is continuously rotated azimuthally, scan smearing (Doviak and Zrnić, 1993) degrades its native resolution of 0.55°. Furthermore, it generates base data output only every 1° in azimuth. The resulting effective azimuthal resolution is about 1.2°, and the

cross-beam resolution within the critical 11-km radius around the airport is 150 to 610 m. For MPAR, assuming the worst-case (45° off broadside for a four-faced system) beamwidth of 1.4°, the cross-beam resolution is 12 to 270 m. For TMPAR, with the 45° off-broadside beamwidth of 2.7°, the cross-beam resolution is 24 to 520 m. There is no scan smearing effect degrading the native beamwidth, because the phased array beams are held stationary during the data acquisition dwell. Thus, as long as MPAR and TMPAR are located at the airport, their azimuthal resolution will be as good as or better than the TDWR's in the required microburst coverage area.
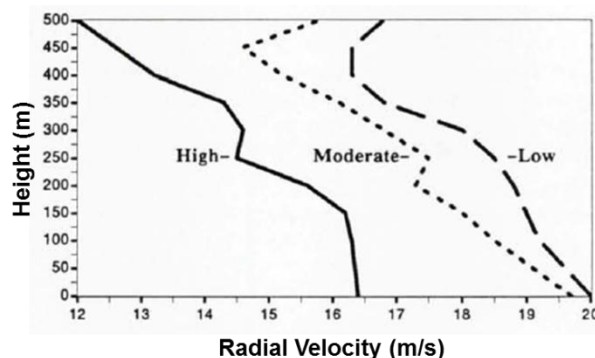

Figure 10. Average differential velocity versus height for low, moderate, and high reflectivity microburst outflows at Denver (Biron and Isaminger, 1991).

Although today's algorithms (MIT, 2007) detect micro-bursts based almost completely on the lowest elevation scans, the upper elevation data are also used in two ways: (1) the presence or absence of significant reflectivity aloft is used to mitigate false alarms and (2) changes in storm cell morphology overhead is monitored to estimate microburst potential, which is then used as an input to the detection module. As discussed earlier, one of the advantages of locating the radar away from the airport is that scans above the airport vicinity can be made without having to tilt the antenna to very high elevation angles. If MPAR is put on the airport, then its beam must be scanned to zenith or an upward-looking antenna face added to cover what would otherwise be a "cone of silence" aloft. Both are feasible but likely costly options.

The cone of silence, though, is a single-radar phenomenon. If neighboring radars provide overlapping coverage of sufficient data quality, then their data can be combined with the on-site radar's data and processed by the wind-shear algorithms. In general, multi-radar mosaics are a good idea and have proven to improve product quality in prototype systems such as the NextGen Weather Processor (NWP) and Gust Front Mosaic (GFMosaic) (Shaw and Troxel, 2002). Even though today's operational wind-shear detection algorithms only use input data from one radar per site, there is no technical reason we could not combine data from multiple radars. In fact, one of the recommended solutions for the potential relocation of the TDWR in New York City was to move it to the John F. Kennedy

International Airport (JFK) and feed in data from the Newark TDWR to cover the cone of silence over the airport (Huang et al., 2009).

To get a rough idea of what the typical distance to the nearest radar would be, we can take the area of the contiguous U.S. (~8 million square kilometers), divide it by the number of full-size MPARs (529) for the all-radar replacement case (Scenario 3) in the 48 states (Cho et al., 2012), and take the square root. The result is 123 km. From this distance, most of the cone of silence (i.e., above 2,900 ft AGL) is covered by the second radar (Figure 11). And the radius of the cone at 2,900 ft AGL is only 1 km.
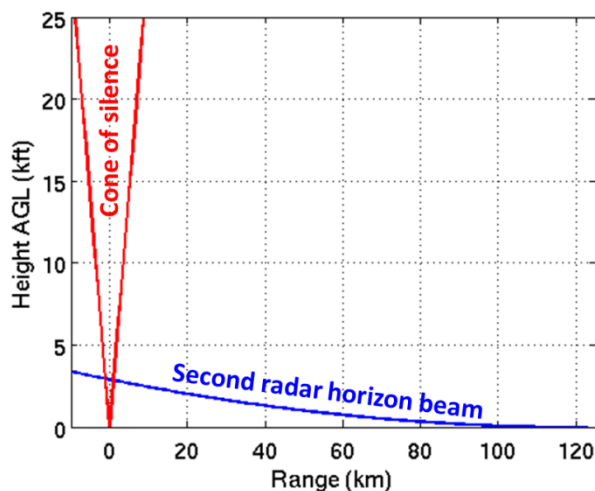

Figure 11. Illustration of cone of silence coverage by a neighboring radar 123 km away. Cone of silence is covered above the blue line. Both radars are assumed to be at the same altitude. The radar maximum elevation angle is 60°.

To precisely quantify the cone of silence coverage by neighboring radars, a table of terminal airspace coverage statistics for the proposed MPAR deployment scenarios and the current radar network was computed and is given in Appendix A of Cho et al. (2013) for TDWR-serviced airports. (Other airports have either no wind-shear detection capability, or coverage by the ASR-9 WSP or LLWAS, which have little or no coverage above the airport; therefore, even a TMPAR will be a definite improvement.) The results were averaged over a cylindrical volume with radius 8 km centered on each airport and extending to 7 km height above ground level. The 7 km limit was chosen because the Integrated Terminal Weather System (ITWS) microburst prediction algorithm has a nominal ceiling of 7 km for its center of mass computation (MIT, 2007). The 8-km radius corresponds to the range at which a 60° elevation angle beam (the assumed MPAR maximum elevation requirement) reaches 7 km altitude. In other words, a radar with a maximum elevation angle of 60° would have an observation gap of 8-km radius at 7-km altitude (a horizontal slice through its cone of silence). The purpose of the table is to show how much of the volume that includes the cone of silence above the MPAR at each TDWR airport would be covered.

The upshot is that, despite the cone of silence over each TDWR airport, inclusion of neighboring radars yields excellent coverage in the airspace aloft. In fact, the volume coverage is 99% or better in almost all cases. (Note that the cone of silence takes up 1/3 of the defined cylindrical volume; thus, if all of the volume was covered except for the cone of silence, the covered fraction would be 2/3 (67%).) The quality of the coverage as indicated by mean horizontal resolution is also excellent, and in most cases exceeds that of the current case, especially when the TDWR is located far from the airport. The worst case for MPAR is San Juan, Puerto Rico (SJU) in Scenario 2 with 80.9% coverage for minimum detectable reflectivity < 5 dBZ. Upon closer inspection, it is revealed that in the siting analysis the nearby NEXRAD site (TJUA) was assigned an MPAR with only three faces (Cho et al., 2012) and a wedge over the airport area aloft was left open. Instead, the aloft coverage is provided by a TMPAR located on St. Thomas, U.S. Virgin Islands (STT), which has a minimum detectable reflectivity above the 5 dBZ threshold at that distance. However, that level of sensitivity should still be adequate for observing storm cells above the airport. And if deemed necessary, a fourth face could be added to the TJUA site. We conclude that the cone of silence for MPARs capable of scanning up to 60° elevation angle will not pose a problem for terminal wind-shear detection performance if the data from neighboring radars are made available for combined processing.

The minimum observation range limit is also a potential problem if MPAR is located on the airport. Due to hardware limitations, radars usually cannot make observations arbitrarily close to the antenna. Over the span of this minimum range limit, there will be a hole in the output data field. With the radar at the airport, this hole will be over a part of the airport. Currently, the minimum range requirement is 500 m for MPAR, which results in a 1-km diameter hole. Even though the cone of silence aloft may be covered by neighboring radars, they will generally be too far away to view near the airport surface, so the hole is left uncovered for wind-shear detection purposes. However, since microbursts have downdraft shafts with a diameter of ~1 km (Mahapatra, 1999), the velocity divergence couplet near the surface spreads out to greater separations distances, for example, as observed by Elmore and McCarthy (1992). Therefore, if a microburst occurs exactly over the 1-km hole, the velocity divergence signature that the detection algorithm needs should be observable outside the hole. There may be a difficulty if the microburst is slightly offset from the hole and one side of the velocity couplet gets obscured. The ASR-9 WSP is located on airports and has a minimum observation range of 500 m, so perhaps data from this system could be used to assess this issue. Alternatively, simulated microburst data could be fed into a microburst detection algorithm to study this problem. As a last resort, if further analysis shows that the minimum observation limit is going to be a serious problem, it is possible to install a minimal LLWAS composed of three anemometers to cover the 1-km diameter hole. This may not be such an expen-

sive solution since the anemometers would be located on the airport property.

The switch from C band (TDWR) to S band (MPAR) presents both advantages and challenges. On the positive side is reduced attenuation through heavy precipitation. Thus, overall data quality will not be degraded as much with MPAR when there is intense precipitation near the radar. Range-velocity ambiguity will also be reduced (Figure 12), so there will be fewer instances of distant weather signal aliasing into the short-range region of interest, and it will be easier to dealias velocity beyond the pulse repetition time (PRT) limited Nyquist interval.
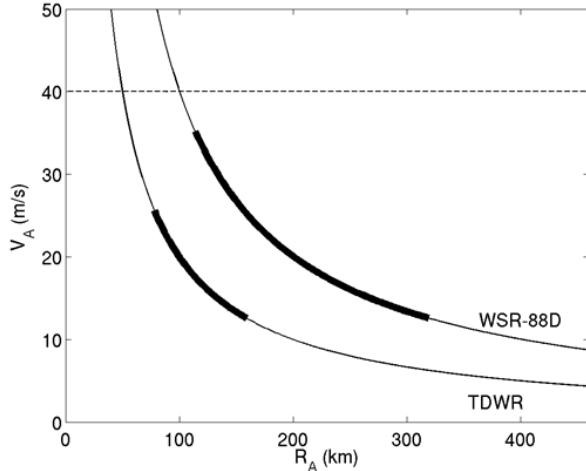

Figure 12. Unambiguous velocity versus unambiguous range for the WSR-88D (NEXRAD) and TDWR (Cho, 2005). The thick lines indicate the operating ranges for velocity estimation mode as bounded on top by the minimum PRT allowed by the transmitter and on bottom by the signal coherency limit. The dashed line at 40 m/s marks the FAA's velocity measurement requirement for the TDWR; the NEXRAD's requirement is 50 m/s. These requirements cannot be met without a velocity dealiasing scheme. Note that the S band NEXRAD allows the simultaneous measurement of larger unambiguous velocity and range than the C band TDWR.

On the negative side will be a decrease in the signal-to-clutter ratio (SCR). The ratio of weather signal to ground clutter signal is given by (Evans and Turnbull, 1989)

$$SCR \propto \frac{\theta_V r Z}{\sigma_0 \lambda^4},\qquad(1)$$

where θ_V is vertical beamwidth, r is range, Z is weather reflectivity, σ_0 is the distributed clutter scattering cross section, and λ is radar wavelength. For a volume-filling weather target, the SCR ratio between two radars is given by

$$\frac{SCR_2}{SCR_1} = \frac{\theta_{V2}\lambda_1^4}{\theta_{V1}\lambda_2^4}.\qquad(2)$$

Consequently, SCR_{MPAR}/SCR_{TDWR} = −9 dB and

SCR_{TMPAR}/SCR_{TDWR} = −6 dB. (As one goes further out in range, microburst outflows and gust fronts stop filling the pulse volume (Figure 6), but at those distances ground clutter will be much weaker because the antenna beam will be higher off the ground.) In any case, this decrease in SCR is a significant disadvantage for clutter filtering with MPAR and TMPAR compared to the TDWR. Furthermore, locating the radar at the airport makes the range to the microburst alert area shorter, which also increases clutter signal strength since more of the antenna main lobe will be in contact with ground structures.

Fortunately, the decrease in SCR can be compensated by using data from higher elevation angles at close range for wind-shear detection. The ITWS machine intelligent gust-front algorithm (MIGFA) already incorporates such a scheme (MIT, 2007). (The wind-shear detection Doppler lidar located at the Las Vegas airport operates with a 2° elevation scan angle to avoid nearby blockage (Keohan et al., 2006)). We need to investigate how well switching between different elevation angle data for near and far range would work in the microburst detector. MPAR should also have the flexibility to form sidelobe nulls against particularly troublesome ground clutter targets and steer finely around terrain contours.

Finally, MPAR will have dual polarization capability that the TDWR does not have. Dual polarization allows better discrimination of target type, which can be an advantage when trying to identify wind-shear phenomena embedded in unwanted clutter signals. For example, bats and birds flying out of a roost may look very much like a microburst based only on reflectivity and velocity fields. However, it is possible that their dual polarization signature differs significantly from that of a microburst outflow, thus helping to reduce false alarms. Identifying hydrometeor types aloft helps characterize the stage of storm cell evolution and may aid in microburst prediction. Dual polarization, though, cannot be expected to compensate for lack of radar sensitivity. For example, a TMPAR would not be able to observe dry microbursts well even with dual polarization. The signal must be observable before it can be exploited by any technique.

In the MPAR siting study, full-size MPARs were placed to cover the 46 airports currently served by the operational TDWRs (Cho et al., 2012). This conservative approach was taken given all the wind-shear detection issues discussed in this section. However, it can also be deduced from the discussion above that it may be acceptable to deploy scaled down TMPARs at TDWR airports that do not suffer from dry microbursts. Since only four of them (Denver, Las Vegas, Phoenix, and Salt Lake City) are considered to be dry microburst sites, considerable cost savings might be realized with such a deployment strategy. Given the safety-critical nature of the mission, an experimental demonstration confirming the soundness of this approach was deemed to be prudent. The next section discusses such an experiment conducted in Oklahoma in the spring of 2012.

3. 2012 OKLAHOMA WIND-SHEAR DETECTION EXPERIMENT

The primary objective of this experiment was to compare microburst prediction and detection performance of the Oklahoma City TDWR (OKC) with the NWRT. The NWRT was essentially a proxy for a TMPAR. However, although the NWRT is similar in sensitivity and beamwidth to the TMPAR, it does not have the dual polarization capability that TMPAR is projected to have. Therefore, we also collected data from nearby dual polarization NEXRADs (KCRI and KOUN) and OU's portable X-band dual polarization radar, the PX-1000 (Cheong et al., 2012), in order to investigate this aspect of TMPAR performance. Here we will only report on the results of the NWRT and TDWR data analysis. The dual polarization study will be conducted in the future.

3.1 Experiment Description

The NWRT is located in Norman, Oklahoma, with an antenna altitude of 370 m above mean sea level (AMSL). The OKC TDWR is just 6 km northwest of the NWRT, with an antenna altitude of 384 m AMSL. The TDWR scans regularly through 360° in azimuth, while the NWRT has a 90° azimuth scan sector that can be rotated mechanically to point to the region of interest.

Operational TDWRs like OKC utilize two volume scan strategies—monitor and hazardous. The former is used during times of calm weather, and when significant convective activity is observed by the radar the scan strategy automatically switches to the latter. Since this experiment focused on periods of severe storms, the hazardous volume scan (Table 1) was usually in effect for the TDWR. Note that there was one long-PRT cut to observe unambiguously to 460 km in range. Cuts 2 and 3 were repeated at the same elevation angle, but with different PRTs for optimal velocity dealiasing. The surface (0.5° elevation angle) was revisited every ~1 minute, and the volume was scanned every ~2.5 minutes. Azimuthal base data samples were output every 1°, and the range resolution was 150 m.

Table 1. OKC TDWR Hazardous Scan Strategy

Cut	Elevation (deg)	Rotation Rate (deg/s)	PRT (µs)
1	0.6	21.6	3066
2	0.5	21.6	598
3	0.5	21.6	838
4	1.0	21.6	598
5	2.5	26	598
6	5.1	30	598
7	0.5	21.6	598
8	7.7	30	598
9	11.3	30	598
10	15.3	30	538
11	0.5	21.6	598
12	20.7	30	518
13	28.2	30	518
14	2.5	30	598
15	0.5	21.6	598
16	5.1	30	598
17	7.7	30	598
18	11.3	30	598
19	0.5	21.6	598
20	15.3	30	538
21	20.7	30	518
22	28.2	30	518
23	0.5	21.6	598

The NWRT had two volume scan strategies designed for this study: EnhancedVCP12_CLEAN_AP and EnhancedVCP12_CLEAN_AP_uniform. The CLEAN_AP extension indicates that the number of pulses was selected to optimize performance of the real-time ground-clutter contamination mitigation filter developed by Warde and Torres (2010). Range oversampling was also implemented to improve data quality and reduce scan time (Curtis and Torres, 2011). Both scan strategies used 50% azimuthal overlapping at all elevations and had a Nyquist velocity of about 29.2 m/s. (The azimuthal beamwidth varied from 1.5° at broadside to 2.1° at 45° off axis.) The EnhancedVCP12_CLEAN_AP scanned 19 elevations from 0.51° to 52.9°, employed split-cut sampling through 6.4°, and had a minimum observation range of 10 km (Table 2). The volume scan time was 64 s and the range resolution was 240 m. This scan strategy was used when storms existed outside of the maximum unambiguous range (117 km) to mitigate second trip returns. Otherwise the uniform-PRT version of the scan strategy was to be used to decrease the minimum observation range from 10 to 3 km and the scan time from 64 to 46 s. However, during the wind-shear events analyzed in this report, EnhancedVCP12_CLEAN_AP_uniform was never used.

Table 2. EnhancedVCP12_CLEAN_AP Scan Strategy

Cut	Elevation (deg)	PRTs (µs)
1	0.5	3000, 800
2	0.9	2912, 800
3	1.3	2624, 800
4	1.8	2320, 800
5	2.4	2016, 800
6	3.1	1736, 800
7	4.0	1456, 800
8	5.1	1208, 800
9	6.4	1016, 800
10	8.0	824
11	10.0	800
12	12.5	800
13	15.6	800
14	19.5	800
15	23.4	800
16	28.2	800
17	34.3	800
18	42.8	800
19	52.9	800

The NWRT ran the adaptive digital signal processing algorithm for PAR timely scans (ADAPTS; Heinselman and Torres, 2011) on both scan strategies. ADAPTS conducted a complete volumetric scan periodically (every 10 minutes by default, definable by user). In between the complete scans, beam positions that were deemed to be devoid of significant weather were turned off based on continuity criteria in order to speed up the scan update rate.

Given the interest in low-altitude wind-shear detection, data collection focused on storms observed within 60 km of the OKC TDWR. For microburst detection, the lowest elevation scan was most critical, because the potentially damaging winds and associated wind shift occur near the surface. Both the TDWR and NWRT provided rapid updates (~1 min) of the lowest elevation scan, which is desirable due to the relatively short lifetime of microbursts. The NWRT had a denser and more rapid vertical sampling of mid-to-upper altitude radar-based precursors necessary for microburst prediction.

The data collection experiment officially ran from 16 April through 30 June 2012, although there were valuable data collected just a few days prior to the kickoff. Within most of this period, daily microburst forecasts were provided by the project meteorologist to assist decisions regarding scheduling of NWRT radar operations. Each week two scientists were scheduled to operate the NWRT, 24 hours a day, 7 days a week. Collaborators were informed of the onset and end of NWRT operations via e-mail. Further details of the experiment can be gleaned from Heinselman et al. (2012).

3.2 Introduction to the Evaluation

Viewing NWRT as a proxy for TMPAR, our goal here is to evaluate the suitability of NWRT base data for the detection of surface wind shear. We want to get a sense of the potential TMPAR POD for microburst detection and gust-front detection. We make no attempt here to assess potential probability of false alarm (PFA). Such an exercise would entail analyzing the NWRT base data for apparent gust front or microburst evidence in scenarios wherein the relevant shear is not actually present. However, labeling a signature as "apparent evidence" is more a function of the way the algorithms are tuned than it is an intrinsic attribute of the data itself. Since we haven't put the NWRT algorithms through a fine tuning, a PFA estimation exercise is therefore not feasible.

We use the OKC TDWR base data quality (and not the ITWS algorithm performance) as truth, with some modifications for situations where NWRT data appears to capture surface events that are missing in the TDWR data. We then compare the NWRT base data to our TDWR truth, and perform a POD calculation to quantify this comparison. A secondary component of this analysis is wind-shear detection software that has been adapted to run on NWRT base data.

The details of this approach are presented below.

3.3 Methodology for Evaluating NWRT Base Data Suitability for the Detection of Surface Divergence and Convergence

As a component of this evaluation, we have adapted two of our standard wind-shear detection software tools to run on NWRT base data. The programs are MIGFA, which detects surface convergence in base data images (and is normally optimized for gust-front detection), and the Automated Microburst Detection Algorithm (AMDA), which detects surface divergence in base data images (and is normally optimized for microburst detection). The NWRT version of MIGFA is very similar to the ITWS version; and AMDA uses the same fundamental divergence-segment-based algorithm as the ITWS divergence detector MBDetect.

3.3.1 Detection Algorithm Issues

We didn't pursue major algorithm tuning of MIGFA and AMDA, which on first consideration one might have thought would yield a direct probabilistic base data quality comparison, nor did we pursue the option of running NWRT base data through the ITWS algorithms. We instead prepared minimally tuned versions of MIGFA and AMDA, suitable for detecting obvious wind-shear candidates, and which we used as described in Section 3.3.2 below. The reasons we didn't pursue fine tuning are described in the following subsection.

3.3.1.1 Optimal or fine tuning of the algorithms would be a significant task in itself

a) The lower NWRT sensitivity would require extensive MIGFA tuning.
b) MIGFA code modification would be required to deal with NWRT wedge boundary effects.
c) With regard to the ITWS algorithms: The very short elapsed times associated with NWRT elevation tilts and volume scans would necessitate extensive general ITWS tuning, and perhaps code modification, to get ITWS MIGFA and MBDetect to run at all.

In practice, a type of gust front that is frequently encountered by MIGFA entails reflectivity imagery in which the leading edge of a front, propagating out into the ambient (often clear) atmosphere, shows a telltale thin-line signature. In the data set analyzed for this report, there are very few cases like this. (Figure 13 shows this phenomenon, in one of the few such cases we encountered.) Consequently, using this data set, unbiased MIGFA tuning could really not be undertaken.
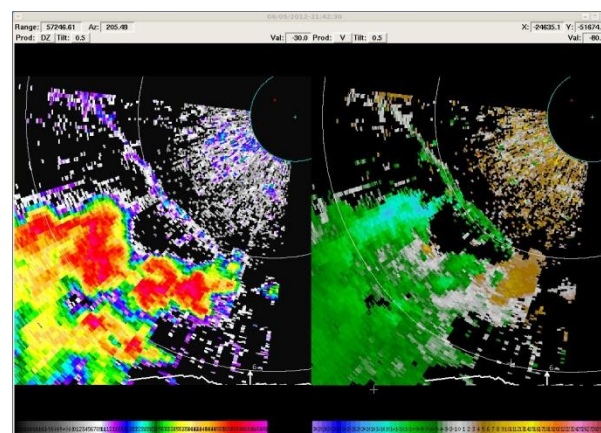

Figure 13. Thin line signatures in both reflectivity (left) and velocity (right) identify the leading edge of a gust front. NWRT 0.5° elevation tilt, 5 June 2012, 21:42 UT.

3.3.1.2 Even if we carried out optimal or fine tuning the result would not likely yield an "apples-to-apples" comparison of base data quality

a) Because NWRT provides no data outside the wedge of observation or inside 10 km in range, the NWRT algorithms are presented with atmospheric contexts that are very different from the ITWS contexts. Such contexts play a significant role for both MIGFA and AMDA.

b) The NWRT and OKC TDWR are not colocated (they are 6 km apart), and that especially compromises comparisons of the presence of gust-front evidence, since a short-range convergence signature that is radially aligned for one radar may have a better cross-radial orientation for the other. (Radial alignment implies little or no Doppler convergence signature. Such signatures play a key role in MIGFA.)

c) Time differences in data acquisition can affect algorithm performance, especially in the detection of microbursts, which can be fast-changing and short-lived.

d) NWRT MIGFA and AMDA will not have the ITWS tracking history; that is, the context for these algorithms differs not only spatially (as pointed in Section 3.3.1.2 (a)) but temporally as well. Both MIGFA and AMDA are very sensitive to differences in tracking history.

3.3.1.3 Extrinsic vs. intrinsic issues

We must take care to separate the extrinsic issues described in Section 3.3.1.2 from intrinsic issues, which in fact are the sources of the data quality differences that we are trying to evaluate. These intrinsic matters include:

a) NWRT-vs.-TDWR beamwidth differences. The TDWR beamwidth is 0.55° x 0.55°, and the NWRT broadside width is 1.5° x 1.5°. Although this difference can occasionally represent an advantage for NWRT (for example, when wind velocity increases in speed with elevation), this will normally result in a TDWR advantage. The attendant problems for NWRT, already described in Section 2, can be particularly pronounced in strong vertical shear environments wherein velocities weaken in strength or change direction with elevation, particularly for events at a distance from the radar, or in shallow boundary layer environments. Figures 14 and 15 show the associated beam-filling differences.

b) NWRT-vs.-TDWR sensitivity differences. The TDWR sensitivity is -19 dBZ at 20 km, but the NWRT sensitivity is 0 dBZ at 20 km. The attendant data quality issues are illustrated in Figure 16.

c) Differences in attenuation through precipitation, and differences in range folding, which are associated with NWRT-vs.-TDWR wavelength differences. These differences, unlike those noted in (a) and (b), represent NWRT advantages. (NWRT is S band and TDWR is C band.) We see these differences in Figure 17.
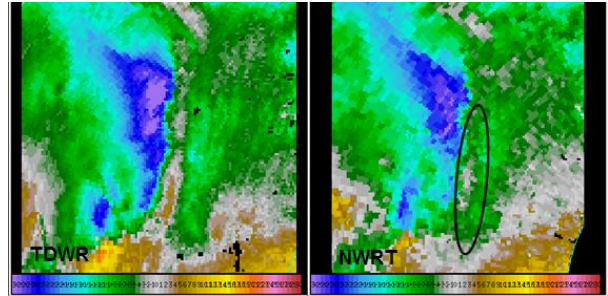

Figure 14. Wider NWRT beam (right) results in weaker shear (circled in black) than is presented in the TDWR base data (left). Data from 0.5° elevation cuts, 30 May 2012, 02:48 UT.
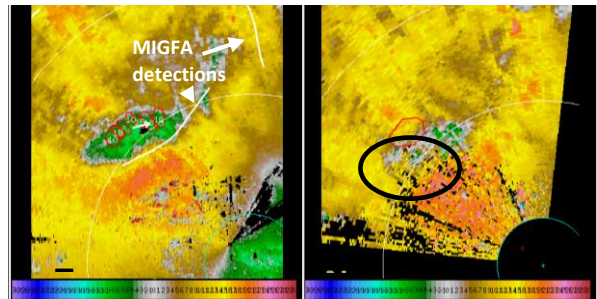

Figure 15. Wider NWRT beam (right) results in weaker convergence line (circled in black) than is presented in the TDWR base data (left). Data from 0.5° elevation cuts, 30 May 2012, 01:54 UT.
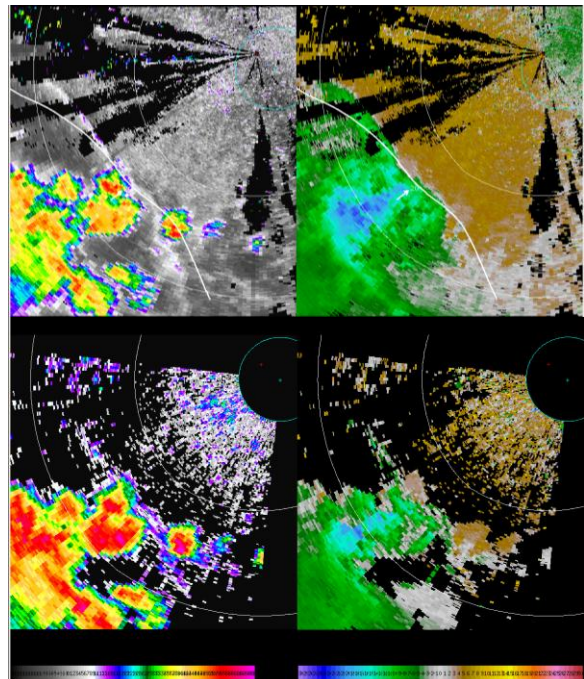

Figure 16. The white boundary in the upper images indicates a TDWR gust-front detection. Lower NWRT sensitivity at this distance (47 km), lower images, interferes with MIGFA's ability to detect this front. Data from 0.5° elevation cuts, 5 June 2012, 21:24 UT. Left-hand plots are reflectivity, right-hand plots are velocity.
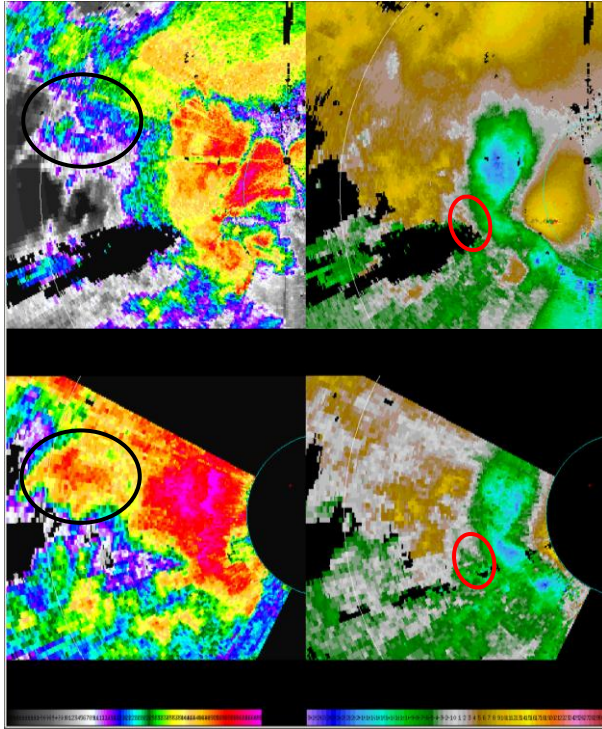
Figure 17. The TDWR (upper images) is unable to detect a cell (region circled in black in left-hand images) because of greater precipitation attenuation, and loses a convergence signature (circled in red in right-hand images) because of range-folding-associated data censoring. These effects are more pronounced in the TDWR data because of its shorter wavelength. Data from 0.5° elevation cuts, 13 April 2012, 20:48 UT. Left-hand plots are reflectivity, right-hand plots are velocity.

3.3.2 Methodology

As we stated in Section 3.1, we have undertaken this study with the idea of letting TDWR base data represent "truth," with occasional modifications wherein NWRT data clearly shows events that are not apparent in the TDWR data (see Figure 17, for example). Historically, in evaluating wind-shear algorithm performance, we measure, or "score," algorithm POD and PFA based on the notion of wind-shear *occurrence*: a single microburst signature in a single surface elevation tilt of data, or a single (section of a) gust-front signature in a single surface elevation tilt of data. In these typical evaluation exercises, there is presupposed an independent notion of "true" event; and POD is then the fraction of occurrences that are detected, while PFA is the fraction of candidate occurrences that are not in fact occurrences in our sense. For example, this describes our approach in evaluating and tuning wind-shear algorithms in the WSP and ITWS systems. In the present study, in order to mitigate the bias associated with our relying on one of the data sets under comparison as the source of truth, and in an effort to mitigate the effects we described in Section 3.3.1.2, we try to keep our notion of (true) event as global as possible. Therefore, we view (in the course of truthing, not scoring) an event as a contiguous region

of surface divergence or convergence, typically (in this data set) associated with a cluster or line of storms, and tracked over time.

3.3.2.1 Scoring

With the considerations of Section 3.3.2, our method is to observe the way the ITWS algorithms (running on OKC TDWR data) are able to track and measure such an event, and then to determine whether algorithms running on the NWRT data could, *in principle,* "keep up" with ITWS performance. (We will elaborate on this in the next paragraph.) Ultimately, our scoring analysis— that is to say, the POD calculation—is not so different from the classical calculation described in Section 3.3.2 (perhaps there are isolated signatures that are not counted as true that otherwise would have been), but nonetheless our broadened notion of "true event" helps guide our truthing analysis, in the absence of inde-pendently determined "true" events, by supplementing a localized analysis with a higher level event-oriented context for our truthing decisions.

To say that algorithms operating on the NWRT data can "keep up" means that the algorithms can track the events tracked by ITWS, without penalty for dropping of detections for the reasons listed in Section 3.3.1. To say that the algorithms can *in principle* keep up means that the data are evaluated to determine whether AMDA and MIGFA, optimally tuned, would make the requisite detections. This assessment is made visually on a scan-by-scan basis, by Lincoln staff who are familiar with the workings of MIGFA and AMDA. As part of this process, the minimally tuned MIGFA and AMDA have been run on the data, and, as a "sanity check," we determine whether these algorithms have detected the stronger wind-shear signatures. This "sanity checking" is the primary benefit we derive from the NWRT algo-rithms. (We have observed that, even minimally tuned, NWRT AMDA does a creditable job. For example, Figure 18 illustrates a good AMDA speed-shear detec-tion.)
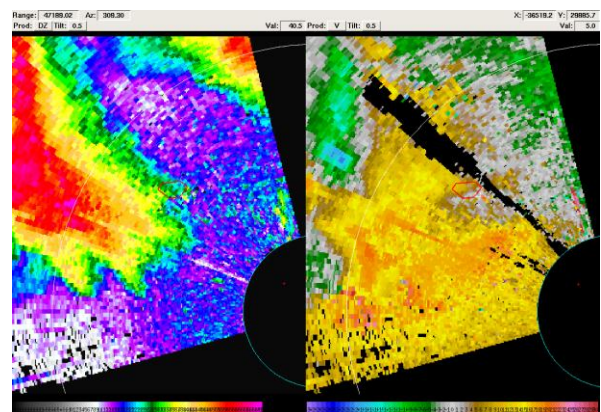

Figure 18. NWRT AMDA speed-shear microburst detection, indicated by red polygon for 0.5° elevation tilt, 30 May 2012, 02:22 UT.

3.3.2.2 Regions of interest

Our region of data collection is shown in Figure 19. The

inner blue region is the microburst-detection region. The locations in this region are all within 35 km of both radars, and at least 10 km from the NWRT. The union of the green and blue regions represents the gust-front-detection region. The locations in this region are all within 60 km of both radars, and at least 10 km from the NWRT.
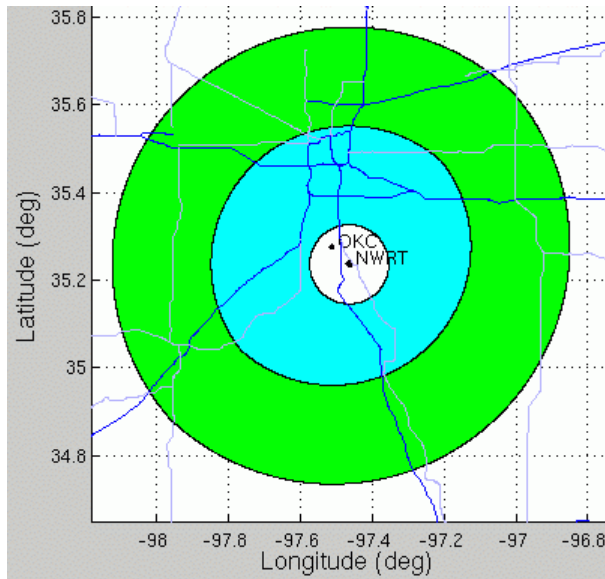

Figure 19. The blue area is the microburst detection region. The union of blue and green represents the gust-front detection area.

3.4 Results

We tabulate here the cases under analysis and the results of our analysis.

3.4.1 Wind-shear Events

Table 3 tabulates the events evaluated in this study. "Events" here refers to our broadly defined truthing events. All microbursts were wet microbursts. See Section 3.3.2.

3.4.2 Results

Figure 20 contains our results. As we have noted, we are presenting here an estimate of potential POD. We have included, for the sake of completeness, the actual POD of the minimally tuned NWRT algorithms. Our "MB" category comprises the standard FAA definition of a microburst-level alert—a wind-shear event producing headwind loss in excess of 30 kt. "WS" refers to the FAA standard divergent wind-shear alert category—wind-shear events producing headwind loss between 15 and 30 kt. Of the microburst samples analyzed for this study, 35% were in the MB and 65% were in the WS category. Although there is only one FAA convergent wind-shear alert category (events producing headwind gain in excess of 15 kt), we have put convergent wind-shear events into two categories—"GF-Strong" refers to wind-shear events producing headwind gain in excess of 30 kt. "GF-Weak" refers to wind-shear events pro-

ducing headwind gain between 10 and 30 kt. Our intent here is to separate safety-critical convergence events from weaker events whose significance primarily relates to such airport operations as choice of runway configuration. Of the gust-front samples analyzed for this study, 67% were in the strong category and 33% were in the weak category.

Table 3. Evaluated Wind-shear Events

Date (2012)	Time Period (UT)	# MB Events	# GF Events
13 April	2013–2118	1	1
14 April	0325–0634	1	1
15 April	0802–0945	1	3
20 April	0048-0454	2	5
29 April	0401-0440	1	1
1 May	0449-0532	4	0
20 May	0421–0643	5	2
29 May	0048–0337	9	4
30 May	0011–0313	10	9
31 May	0335–0551	2	1
5 June	2100–2318	1	1
9 July	2039–2238	4	N/A*
10 July	1831–2042	10	1
Total		51	29

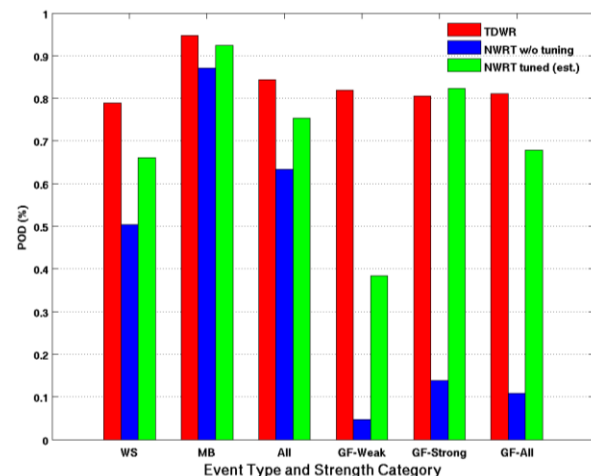*Gust-front events not evaluated due to MIGFA processing errors with NWRT data.

Figure 20. POD results of the study.

For reference, past TDWR microburst detection performance evaluations yielded PODs ranging from 92% to 95% at wet microburst sites (Evans and Weber, 2000), so our OKC TDWR microburst POD matches up quite well.

The tuned POD estimates in Figure 20 are necessarily qualitative and are based on our experience in tuning these algorithms on other platforms. One must keep in mind as well that the "wedge" limitations described in Section 3.3.1.2, which would require NWRT-specific

tuning to overcome, would not apply to MPAR itself. (Because MPAR data would be free of these wedge artifacts, one could fairly estimate that MPAR MIGFA would perform better than NWRT MIGFA.) This particular element of tuning would entail introducing a type of adaptive image masking which is not currently present in MIGFA, and which would therefore involve (perhaps extensive) code modification.

To address the issues described in Section 3.3.1.3, we estimate that a MIGFA tuning procedure would include at least the following elements:

a) To address data quality issues associated with beamwidth differences, we may wish to weight reflectivity-based gust-front evidence higher than Doppler-based evidence, and to give greater weight to evidence of signature motion.

b) To address data quality issues associated with lower NWRT sensitivity, we may wish to modify the MIGFA image template-matching mechanism to become more sensitive with range. This notion of adaptively modifying image templates based on range is not currently a feature of MIGFA, and so would require code modification.

Given that the NWRT AMDA performance is already reasonable, an AMDA tuning procedure would entail a close analysis of particular cases to determine whether improvements could be made through small modifications of the basic parameters, like shear segment length, duration, or clustering values; and whether attendant false alarm suppression might be gained through modification of some of the secondary parameters, like storm core shape.

Finally, we must emphasize that a truly satisfactory tuning must be based on a large data set, in which a wide variety of wind-shear phenomena are present, as well as a variety of local weather patterns that do not represent surface shear, but could be mistaken by the algorithms for such patterns.

4. MICROBURST PREDICTION

One of the clear advantages that MPAR has over TDWR is its ability to scan through a volume rapidly. This capability can make a big difference in the realm of microburst prediction. Microburst detectors look for divergent wind patterns just above the ground surface, but by the time this signature becomes apparent the aviation hazard is already fully present. Since the source of the downburst that generates the surface divergence is aloft, it is possible to monitor the 3D volume of an evolving storm to deduce that a downdraft capable of producing a microburst is in progress. In theory, the more frequently the storm morphology evolution is updated, the better the microburst prediction algorithm ought to work. Adaptive scanning with MPAR could also allow enough time to scan the targeted volume without gaps in elevation angle or at least fewer gaps (Table 2) than the TDWR scan strategy (Table 1). With this in mind we took an initial step toward applying rapid-scan phased array radar data to microburst prediction.

Key radar-observable microburst predictors are a reflectivity core aloft, descent of the core, mid-level convergence, and vorticity associated with the convergence (Figure 21).
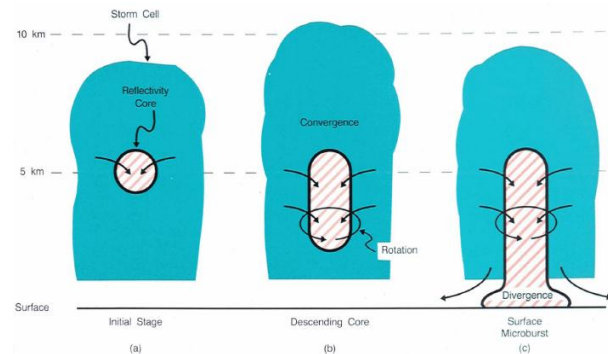

Figure 21. Stages in the evolution of a microburst. (a) A reflectivity core initially forms aloft at 5 to 10 min prior to the onset of surface outflow. (b) As the downdraft develops, the core descends, and convergence and rotation develop. (c) Finally, the core reaches the surface and the surface outflow begins. From Merritt et al. (1989).

MIT LL developed an automated microburst prediction module (Wolfson et al., 1994) for ITWS, which uses TDWR data as input. Briefly, the algorithm looks for identifying features in the growth, downdraft, and transition phases of storm evolution, with the descent of the vertically integrated liquid water (VIL) center of mass as one of the key indicators (Figure 22). Atmospheric sounding profiles derived from radiosonde and aircraft measurements are also used to assess the thermodynamic stability of the storm environment. ITWS, however, does not output microburst predictions. The predictions are only used internally to aid the microburst detection algorithm in making more accurate alerts, and the gain in detection performance is estimated to be just 1-2% on a hit by hit, not event, basis (Huang et al., 2009). The reasons for the rather weak contribution of the microburst prediction module are thought to be because (1) the detection probability rate is already very high without the prediction input and (2) the 2.5-minute volume scan update rate of the TDWR is not fast enough to reliably catch the microburst precursors.

Initially we attempted to adapt and feed NWRT data into an off-line ITWS test string, but we discovered that this approach would require more resources than we had available for this project. So instead, we constructed a prediction model in Matlab, which we describe below.

The framework of our prediction model was to generate microburst precursor interest fields, combine them in a fuzzy logic fashion, then threshold the resulting field to generate predictions (Figure 23). This structure allows straightforward insertion of new interest fields in the future when, for example, dual polarization parameters might be included to boost performance.
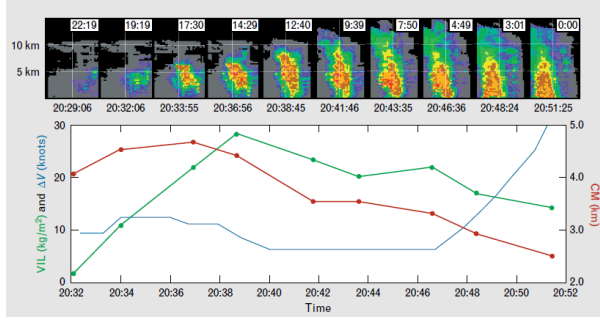
Figure 22. An evolving thunderstorm that occurred in Orlando on 14 July 1994: (Top) radar vertical cross sections with the time to microburst onset listed at the top of each frame, and (bottom) measurements of the VIL shown in green, the height of the center of mass shown in red, and the speed of the microburst differential outflow shown in blue, as a function of time for the cells shown at the top. Each data point represents an average for the cell at that time. Note that VIL increases monotonically, and that the center of mass changes little at first but then drops rapidly after VIL has peaked. These changes are precursors to the microburst, which does not occur until the very end of the frame sequence (from Wolfson et al., 1994).
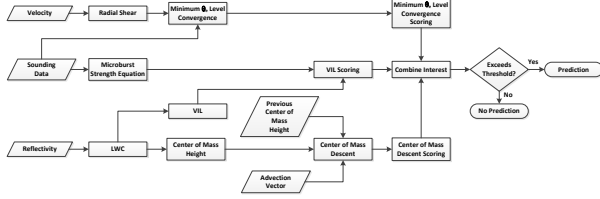

Figure 23. Simplified flow chart of the Matlab-based microburst prediction algorithm.

For the interest fields we selected (1) VIL, which gives an indication of the source of potential energy available to drive a downdraft, (2) wind convergence at the height of the minimum in the equivalent potential temperature (θ_e) profile, which is the intake air source for the downdraft (e.g., Atkins and Wakimoto (1991)), and (3) vertical descent in the liquid water content (LWC) center of mass (CM), which is an indication of the downdraft initiation that eventually results in hazardous wind divergence near the ground surface. (1) and (3) are quantities that are computed and used in the ITWS microburst prediction algorithm, but (2) is not. Below we discuss each field.

VIL by itself is not a good measure of microburst potential—the background thermodynamic stability of the atmosphere must also be taken into account. Therefore, in computing the VIL interest field, we utilized adaptive parameters VIL$_{weak}$ and VIL$_{strong}$ in the equation

$$VIL_{Int} = \frac{VIL - VIL_{weak}}{VIL_{strong} - VIL_{weak}} , \qquad (3)$$

where VIL$_{weak}$ and VIL$_{strong}$ were calculated from the microburst strength equation (MIT, 2007)

$$VIL_{weak|strong} = \left(\frac{1132 v_{out}^2}{h_f \Gamma_e^3 R^2} - 51.1 \Gamma_e + 340 \right)^{2/3}, \quad (4)$$

and

$$R = 1 + \left(\frac{\Gamma_{el}}{\Gamma_e} - 1 \right) \ln 10 , \qquad (5)$$

where Γ_e is the mean (surface to h_f) equivalent potential temperature lapse rate (K/km), Γ_{el} is the low-level (surface to $0.75 h_f$) equivalent potential temperature lapse rate (K/km), h_f is the freezing level (km), and v_{out} is the microburst outflow strength set to 7.5 m/s for VIL_{weak} and 15 m/s for VIL_{strong}. In Equation (3) VIL_{Int} was only allowed to range between 0 and 1; negative outcomes were reset to 0 and outcomes greater than 1 were reset to 1.

The wind convergence ((m/s)/km) was first computed along the slant radials and then resampled in 3D Cartesian space like the other quantities. This does not strictly yield horizontal convergence, but is close at low elevation angles. For our exploratory purposes, it was deemed close enough. The convergence interest was computed from the altitude slice of the convergence field, C, matching the height of the minimum in the θ_e profile using the equation

$$C_{Int} = \frac{C_2 - C}{C_2 - C_1} . \qquad (6)$$

Again, C_{Int} was only allowed to range between 0 and 1; negative outcomes were reset to 0 and outcomes greater than 1 were reset to 1. The tunable parameters C_1 and C_2 were set to -5 (m/s)/km and -3 (m/s)/km, respectively.

For each volume scan a 3D LWC field was computed from the Cartesian-gridded reflectivity data. Then the LWC CM height field was computed up to a ceiling of 7 km. The CM vertical motion, W (m/s), was then computed from the difference between two consecutive volume scans. However, in order to remove effects from horizontal advection, we shifted the initial CM field using the first-order tracking vector computed by a field alignment algorithm run on the two consecutive CM images (Ravela et al., 2007). The vertical motion field was then smoothed by a 2D Gaussian filter before being converted to an interest field by

$$W_{Int} = \frac{W_2 - W}{W_2 - W_1} . \qquad (7)$$

Again, W_{Int} was only allowed to range between 0 and 1; negative outcomes were reset to 0 and outcomes greater than 1 were reset to 1. The tunable parameters W_1 and W_2 were set to -6 m/s and -3 m/s, respectively.

The three interest fields were then combined using the MIN operator with the rationale of trying to minimize false alarms as much as possible. Intermediate microburst predictions were generated at points where the combined interest field exceeded 0.5. However, in an effort to further reduce false alarms, we implemented a rudimentary persistence check before issuing a final microburst prediction.

The intermediate microburst predictions were evaluated using a spatial grid (1 km x 1 km) coarser than the data grid. If more than half of the points within an evaluation cell had positive intermediate predictions, than that cell

was marked a hit. However, a final prediction was not issued unless the same cell was a hit for two consecutive times. The prediction was then advected forward to the next time using the tracking vector.

Vertical soundings of temperature and humidity needed to calculate h_f, Γ_e, and Γ_{el} were taken from the twice-daily rawinsonde launches from station OUN that was closest in time to the analyzed data. Clearly, this was not ideal since a difference of up to six hours could be present between the sounding and the radar observation. In the future, if the algorithm were to be incorporated into ITWS, it would then have access to better thermodynamic information assimilated from rawinsonde, aircraft, and numerical weather model data.

Since we did not have the same computational constraints as the operational ITWS, we set the horizontal and vertical resolution of the resampled 3D Cartesian data to 250 m (it is 1 km in the ITWS microburst prediction program). Also, to provide a simulated comparison between the NWRT and TDWR, we fed the algorithm with the full time and spatial resolution NWRT data and with the data subsampled to no less than 2.5 minutes apart and the elevation angle cuts matched closest to a TDWR hazard scan set. Below we show some example results.

In Figure 24, the left two panels show the lowest-elevation-angle reflectivity (top) and radial velocity (bottom). The other panels show the interest fields as indicated. The red triangle in the velocity plot indicates a microburst prediction. The time is 19:45:43 UT.

In Figure 25, the time is 19:50:15 UT and the first detection (magenta circle) of the microburst predicted in Figure 24 is observed. That is a lead time of 4.5 minutes. (The microburst detection algorithm used was a Matlab version of the ITWS microburst detection algorithm.) There is another microburst prediction closer to the center of the figure; this prediction was actually issued at 19:49:41 UT, one time stamp previous to the one shown in Figure 25.

Figure 26 shows the first microburst detection corresponding to the upper prediction location in Figure 25. The time is 19:52:11 UT, so the lead time for this one was 2.5 minutes. There were no false alarms for the duration of this data set. OUN sounding data from 11 July 2006 at 0 UT was used to derive Γ_e = 5.1 K/km, Γ_{el} = 5.5 K/km, h_f = 4.95 km, and θ_e minimum at 6 km height above ground level.

When the same data as shown in Figures 24 to 26 were subsampled in time and elevation to mimic a TDWR then fed into the microburst prediction algorithm, no predictions were generated. Because the volume update rate of the TDWR hazard scan is 2.5 minutes, there was just not enough interest evidence accumulation before the microburst actually occurred.
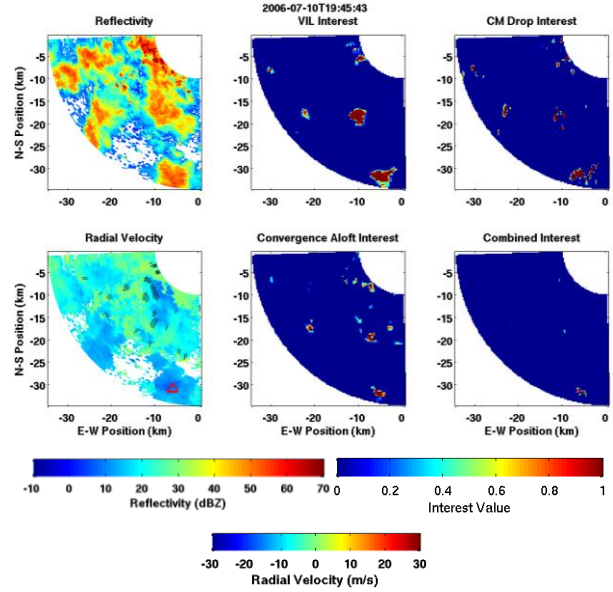

Figure 24. Reflectivity (top left) and radial velocity (bottom left) from the 0.5° elevation scan. Microburst prediction is indicated by the red triangle in the velocity plot. Interest fields for VIL (top middle), CM descent (top right), convergence at the minimum θ_e level (bottom middle), and combined (bottom right) are also shown. This data set was collected by the NWRT on 10 July 2006 at 19:45:43 UT. This case was chosen because the descending core was quite clear. The volume scan period was 34 s. Further data collection details are available in Heinselman et al. (2008). The same color bars apply to Figures 25 to 28.
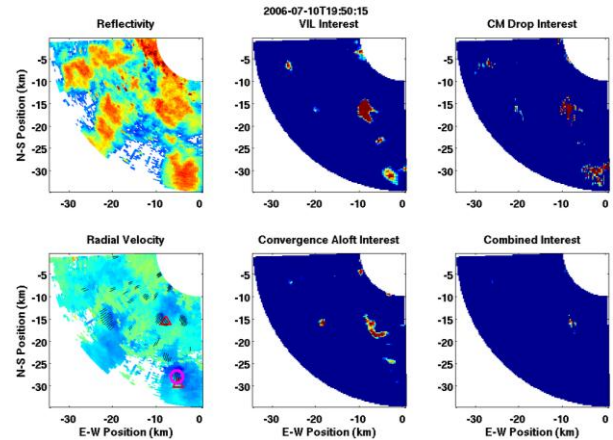

Figure 25. Same as Figure 24 except at 19:50:15 UT. Microburst detection is indicated by a magenta circle.

Another case from 13 April 2012 is shown in Figure 27. On this day OUN sounding data from 14 April 2012 at 0 UT was used to derive Γ_e = 4.5 K/km, Γ_{el} = 3.4 K/km, h_f = 4.06 km, and θ_e minimum at 4.1 km height above ground level. The first microburst prediction for this time period is observed in the velocity plot.
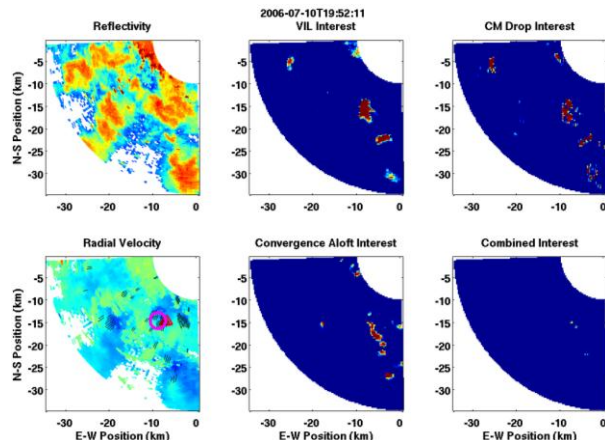
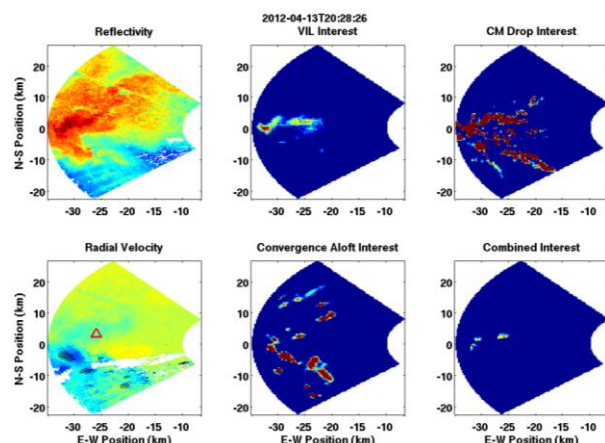*Figure 26. Same as Figure 22 except at 19:52:11 UT.*

Figure 27. Same as Figure 24 except at 13 April 2012, 20:28:26 UT. The volume scan period was 64 s.

The first microburst detection following the prediction in Figure 27 is shown in Figure 28 at 20:39:39 UT. That is a lead time of over 10 minutes. The prediction shown in Figure 28 was soon followed by another microburst detection in the same spot.
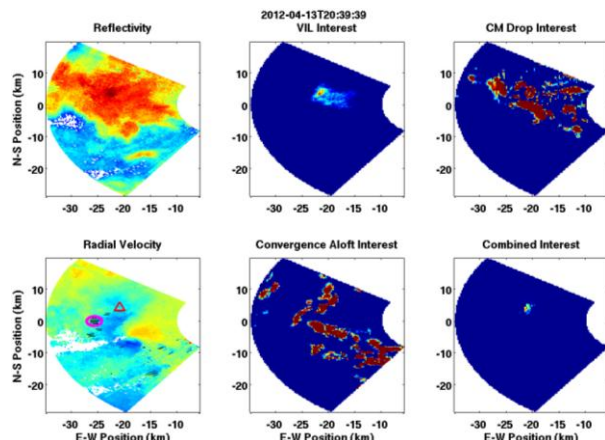

Figure 28. Same as Figure 27 except at 20:39:39 UT.

Note that even though the reflectivity values were generally higher in Figures 27 and 28 than in Figures 24–26, the VIL interest field had lower values. This is because the background stability (according to the closest sounding data) was stronger and thus increased the VIL thresholds of Equation (4). Therefore, accurate knowledge of thermodynamic properties is crucial to microburst prediction and ultimately may be the limiting factor in its success. In fact, applying the prediction algorithm to several other cases, it appeared that a significant number of missed detections and false alarms might be attributed to uncertainty in the stability parameters. To compensate for this uncertainty the operational ITWS microburst prediction algorithm has a feedback mechanism to adjust the sensitivity of the microburst strength equation depending on the performance of the prediction algorithm relative to real-time detections.

This study was only a preliminary attempt at exposing the rapid-scan benefit for microburst prediction purposes. Dual polarization may also aid in identifying microburst precursors aloft through microphysics and downdraft characterizations (Wakimoto and Bringi, 1988). Midlevel rotation could be another value-added interest field (Isaminger, 1988). With data already collected from many other microburst events, this is a topic that can be explored further in a follow-on study.

5. SUMMARY DISCUSSION

In Section 2 we discussed the technical issues associated with wind-shear detection using MPAR. In particular, the risks centered on the scaled-down terminal version (the TMPAR), since it would have sensitivity and spatial resolution inferior to the TDWR. TMPAR's sensitivity would clearly not be good enough for dry microburst detection, but could it perform as well as the TDWR at wet microburst sites? We showed that by locating the TMPAR at the airport instead of at the current TDWR sites, which are 10 to 24 km from the airport, equivalent spatial resolution could be achieved in the required microburst coverage zone. However, unless the TMPAR is required to scan up to zenith elevation angle, there would be a cone of silence above the airport. Fortunately, we were able to show that, given the siting scenarios from a previous study (and assuming a maximum elevation angle of 60°), the resulting cone of silence at TDWR airports could be adequately covered by neighboring radars. In general, the combined use of data from multiple radars should improve the reliability of wind-shear detection compared to the stove-piped single-radar products that are generated today.

The minimum observation range also appeared to pose a risk for on-airport siting. For example, with a minimum range limit of 500 m there will be a 1-km diameter hole in coverage over some section of the airport. However, since most velocity divergence couplets produced near the surface by microbursts exceed 1 km in size, it is not likely that the entire microburst signature will be hidden by the hole. The performance of the ASR-9 WSP at wet microburst sites is encouraging, because it has a 500-m minimum observation range as well as a large cone of silence while being sited on airports. The WSP's

measured POD/PFA for microbursts with velocity differential ≥ 15 m/s are 95%/13% (Huntsville, AL), 87%/15% (Kansas City, MO), and 91%/6% (Orlando, FL) (Weber et al., 1996). With better spatial resolution and sensitivity characteristics, the TMPAR should perform better than the ASR-9 WSP.

Gust-front detection and tracking out to 60 km with the TMPAR was also a concern due to the low reflectivity of gust fronts. For reference, the observed WSP POD/PFA for gust fronts with velocity differential ≥ 15 m/s is 73%/11% at Orlando (Weber et al., 1996). Near-range detection performance would be improved by locating the TMPAR at the airport, but its far-range sensitivity and spatial resolution might be marginal.

To help answer the remaining uncertainties about the wind-shear detection performance of TMPAR at wet microburst sites, we executed a field experiment in Oklahoma. Data were collected by a TDWR and a phased array radar (the NWRT) located 6 km apart. The estimated NWRT POD of over 90% for divergent velocity differential ≥ 15 m/s (with a tuned algorithm) shows that the FAA requirement for microburst detection can be met by a TMPAR at wet microburst sites. This should, in fact, be an underestimate, given that the microburst data collection area was approximately 10 to 35 km from the radar, due to the inability of the NWRT to observe closer than 10 km during this experiment. Since an on-airport TMPAR's required microburst coverage zone would be only within 11 km, it should have much less of the velocity smearing issue noted in Figure 14, and the microburst detection performance, especially for weaker divergence events, should improve.

The NWRT's estimated gust-front detection performance with a tuned algorithm was also comparable to the TDWR's POD for strong events. Weak event performance, however, was significantly inferior relative to the TDWR's. Here, then, is the crux of the issue when considering replacing TDWRs with TMPARs at wet microburst sites. The safety-critical requirement of POD ≥ 90% would likely be met for wet microbursts, but what level of gust-front detection performance is acceptable? The FAA does not have a detection performance requirement for gust fronts, since it is an airport operations efficiency, not necessarily safety, issue outside of the ARENAs. If the "do no harm" approach is taken, i.e., no performance degradation relative to the TDWR is deemed acceptable then TMPAR should not replace the TDWR anywhere; the full-size MPAR should be placed at TDWR airports as was done in the siting study. Ultimately, the decision may be based on a cost-benefit analysis that weighs the relative costs of a TMPAR vs. an MPAR against the delay-reduction benefits provided by different levels of gust-front detection performance. The mechanism is in place to do this, as we have conducted a comprehensive wind-shear system cost-benefit study previously (Hallowell et al., 2009). In that analysis we assumed that terminal operational efficiency would benefit from a maximum of 20 minutes in wind-shift warning time; further assuming a gust-front approach speed of 15 m/s, the resulting

maximum coverage range needed for gust fronts was 18 km. (This is much shorter than the actual operational gust-front product generation out to 60 km from the radar. If 18 km is really the critical range needed for gust-front coverage, then the TMPAR should have adequate sensitivity.) Furthermore, the cost-benefit analysis showed that delay-reduction benefits due to gust-front detection were quite small except at the busiest airports such as the three New York City airports, Atlanta, and Chicago O'Hare. So perhaps the full-size MPARs may only be justified at the dry microburst sites plus the wet microburst airports with the heaviest traffic.

For microburst prediction, we were able to show that the rapid volume scanning capability of a phased array radar could potentially generate a prediction more than ten minutes in advance. Current algorithms, however, are dependent on accurate knowledge of the local thermodynamic stability properties of the atmosphere. Further research is needed to prove that a reliable, robust, and accurate microburst prediction engine can be fielded operationally.

Potential dual polarization benefits for wind-shear detection and prediction are yet to be explored. The data collected during this field experiment by dual-polarized radars (KCRI, KOUN, and PX-1000) should be exploited for this purpose. With dual polarization we anticipate improved false alarm mitigation due to better categorization of scatterers and more reliable microburst prediction.

Finally, let us briefly discuss dry microburst detection. There is concern that because the TDWR has not been meeting the 90%/10% microburst POD/PFA requirement at some of the dry sites, even the full-size MPAR will also not be able to do so. Previous analysis has shown that the problematic dry sites (Las Vegas, Salt Lake City, and Phoenix) have different location-dependent issues (road clutter, birds and bats, terrain-induced shear phenomena and blockages) that degrade the microburst detection performance; Denver is also a dry microburst site, but the TDWR performs very well there because it does not have these particular problems (Cho, 2008). Some of these challenges will be mitigated through advanced signal processing algorithms that are planned to be installed on the TDWR in the future (Cho and Weber, 2010), with our detection performance model predicting microburst POD exceeding 90% at all sites except Las Vegas (Cho, 2008). A full-size MPAR should perform at least as well, and perhaps even better, with the added capability of fine beam steering and pattern control for clutter avoidance, and dual polarization for false alarm mitigation.

6. ACKNOWLEDGMENT

7. REFERENCES

Atkins, N. T., and R. M. Wakimoto, 1991: Wet microburst activity over the southeastern United States: Implications for forecasting. *Wea. Forecasting*, **6**, 470-482.

Benner, W. E., G. Torok, M. Weber, M. Emanuel, J. Stailey, J. Cho, and R. Blasewitz, 2009: Progress of multifunction phased array radar (MPAR) program. Preprints, *25th Conf. on Interactive Information and Processing Systems for Meteorology, Oceanography, and Hydrology*, Phoenix, AZ, Amer. Meteor. Soc., 8B.3.

Biron, P. J., and M. A. Isaminger, 1991: High resolution microburst outflow vertical profile data from Huntsville, Alabama, and Denver, Colorado. Project Rep. ATC-163, MIT Lincoln Laboratory, Lexington, MA, 214 pp.

Cheong, B. L., R. Palmer, Y. Zhang, M. Yeary, and T.-Y. Yu, 2012: A software-defined radar platform for waveform design. Preprints, *2012 IEEE Radar Conference*, Atlanta, GA, 591-595.

Cho, J. Y. N., 2005: Multi-PRI signal processing for the Terminal Doppler Weather Radar, Part II: Range-velocity ambiguity mitigation. *J. Atmos. Oceanic Technol.*, **22**, 1507-1519.

Cho, J. Y. N., 2008: TDWR dry site problem assessment and RDA Software Build 3 recommendation. Project Memo. 43PM-Wx-0107, MIT Lincoln Laboratory, Lexington, MA, 32 pp.

Cho, J. Y. N., and B. D. Martin, 2007: Technical assessment of the impact of decommissioning the TDWR on terminal weather services. Project Rep. ATC-331, MIT Lincoln Laboratory, Lexington, MA, 68 pp.

Cho, J. Y. N., and R. G. Hallowell, 2008: Detection probability modeling for airport wind-shear sensors. Project Rep. ATC-340, MIT Lincoln Laboratory, Lexington, MA, 73 pp.

Cho, J. Y. N., and M. E. Weber, 2010: Terminal Doppler Weather Radar enhancements. *Proc. 2010 IEEE Radar Conf.*, 1245-1249.

Cho, J. Y. N., R. S. Frankel, M. F. Donovan, M. S. Veillette, and P. L. Heinselman, 2013: Wind-shear detection performance study for multifunction phased array radar (MPAR) risk reduction. Project Rep. ATC-409, MIT Lincoln Laboratory, Lexington, MA, 67 pp.

Cho, J. Y. N., S. Huang, and R. Frankel, 2012: NextGen surveillance and weather radar capability (NSWRC) siting analysis. Project Rep. ATC-391, MIT Lincoln Laboratory, Lexington, MA, 124 pp.

Curtis, C. D., and S. M. Torres, 2011: Adaptive range oversampling to achieve faster scanning on the National Weather Radar Testbed Phased-Array Radar. *J. Atmos. Oceanic Technol.*, **28**, 1581-1597.

Doviak, R. J., and D. S. Zrnić, 1993: *Doppler Radar and Weather Observations*. 2nd Ed., Academic Press, 562 pp.

Elmore, K. L., and J. McCarthy, 1992: A statistical characterization of Denver-area microbursts. DOT/FAA/NR-92/13, National Center for Atmospheric Research, Boulder, CO, 54 pp.

Evans, J., and D. Turnbull, 1989: Development of an automated windshear detection system using Doppler weather radar. *Proc. IEEE*, **77**, 1661-1673.

Evans, J. E., and M. E. Weber, 2000: Weather radar development and application programs. *Linc. Lab. J.*, **12**, 367-382.

FAA, 1987: System requirements statement for the Terminal Doppler Weather Radar. Order 1812.9, Department of Transportation, Federal Aviation Administration, Washington, DC, 12 pp.

FAA, 1995: Specification: Terminal Doppler Weather Radar with enhancements. FAA-E-2806c, Department of Transportation, Federal Aviation Administration, Washington, DC, 162 pp.

FAA, 2004: TDWR meteorological products guide. SDR-TDWR-009, Department of Transportation, Federal Aviation Administration, National Airway Systems Engineering Division, Washington, DC, 24 pp.

Forsyth, D. E., J. F. Kimpel, D. S. Zrnic, R. Ferek, J. Heimmer, T. J. McNellis, J. E. Crain, A. M. Shapiro, R. J. Vogt, and W. Benner, 2009: The National Weather Radar Testbed (phased-array)–a progress report. Preprints, *25th Int. Conf. on Interactive Information and Processing Systems for Meteorology, Oceanography, and Hydrology*, Phoenix, AZ, Amer. Meteor. Soc., 8B.2.

Hallowell, R. G., J. Y. N. Cho, S. Huang, M. E. Weber, G. Paull, and T. Murphy, 2009: Wind-shear system cost benefit analysis update. Project Rep. ATC-341, MIT Lincoln Laboratory, Lexington, MA, 186 pp.

Wakimoto, R. M., and V. N. Bringi, 1988: Operational detection of microbursts associated with intense convection: The 20 July storm during the MIST project. *Mon. Wea. Rev.*, **116**, 1521-1539.

Heinselman, P. and S. Torres, 2011: High-temporal resolution capabilities of the National Weather Radar Testbed phased-array radar. *J. Appl. Meteor. Climtol.*, 50, 570-593.

Heinselman, P. L., D. L. Priegnitz, K. L. Manross, T. M. Smith, and R. W. Adams, 2008: Rapid sampling of severe storms by the National Weather Radar Testbed. *Wea. Forecasting*, **23**, 808-824.

Heinselman, P., J. Cho, B. L. Cheong, M. Weadon, M. Emanuel, T. Crum, and P. Biron, 2012: Multifunction Phased Array Radar wind shear experiment. Preprints, *26th Conf. on Severe Local Storms*, Nasheville, TN, Amer. Meteor. Soc., P3.55.

Heiss, W. H., D. L. McGrew, and D. Sirmans, 1990: NEXRAD: Next Generation Weather Radar (WSR-88D). *Microwave J.*, **33**, 79-98.

Huang, S., J. Y. N. Cho, M. F. Donovan, R. G. Hallowell, R. S. Frankel, M. L. Pawlak, and M. E. Weber, 2009: Redeployment of the New York TDWR: Technical analysis of candidate sites and alternative wind shear sensors. Project Rep. ATC-351, MIT Lincoln Laboratory, Lexington, MA, 96 pp.

Isaminger, M. A., 1988: A preliminary study of precursors to Huntsville microbursts. Project Rep. ATC-153, MIT Lincoln Laboratory, Lexington, MA, 28 pp.

Keohan, C. F., K. Barr, and S. M. Hannon, 2006: Evaluation of pulsed lidar wind hazard detection at Las Vegas International Airport. Preprints, *12th Conf. on Aviation Range and Aerospace Meteorology*, Atlanta, GA, Amer. Meteor. Soc., P5.4.

Klingle-Wilson, D., and M. F. Donovan, 1991: Characteristics of gust fronts. Preprints, *4th Int. Conf. on Aviation Weather Systems*, Paris, France, Amer. Meteor. Soc., 387-392.

Mahapatra, P. R., 1999: *Aviation Weather Surveillance Systems.* American Institute of Aeronautics and Astronautics, Reston, VA, 453 pp.

Merritt, M. W., D. Klingle-Wilson, and S. D. Campbell, 1989: Wind shear detection with pencil-beam radars. *Linc. Lab. J.*, **2**, 483-510.

Michelson, M., W.W. Shrader, and J.G. Wieler, 1990: Terminal Doppler Weather Radar. *Microwave J.*, **33**, 139–148.

MIT, 2007: Integrated Terminal Weather System (ITWS) algorithm description. DOT/FAA/ND-95/11 Rev. E, MIT Lincoln Laboratory, Lexington, MA, 2446 pp.

Ravela, S., K. Emanuel, and D. McLaughlin, 2007: Data assimilation by field alignment. *Physica D*, **230**, 127-145.

Shaw, J. D., and S. W. Troxel, 2002: Progress report on the Integrated Terminal Weather Systems GFMosaic algorithm. *10th Conf. on Aviation, Range, and Aerospace Meteorology*, Portland, OR, *Amer. Meteor. Soc.*, JP1.2.

Souders, C., T. Kays, S. Spincic, F. Bayne, C. Miner, S. Abelman, R. Showalter, J. Tauss, L. Leonard, E. Dash, and J. May, 2010: Next Generation Air Transportation System (NextGen) weather requirements: An update. Preprints, *14th Conf. on Aviation, Range, and Aerospace* Meteorology, Atlanta, GA, American Meteorological Society, J4.1.

Warde, D., and S. Torres, 2010: A novel ground-clutter-contamination mitigation solution for the NEXRAD network: the CLEAN-AP filter. Preprints, *26th International Conference on Interactive Information and Processing Systems (IIPS) for Meteorology, Oceanography, and Hydrology*, Atlanta, GA, Amer. Meteor. Soc., 8.6.

Weber, M. E., and M. L. Stone, 1995: Low altitude wind shear detection using airport surveillance radars. *IEEE Aerosp. Electron. Syst. Mag.*, **10**, 3-9.

Weber, M. E., J. A. Cullen, S. W. Troxel, and C. A. Meuse, 1996: ASR-9 Weather System Processor (WSP): Wind shear algorithms performance assessment. Project Rep. ATC-247, MIT Lincoln Laboratory, Lexington, MA, 42 pp.

Weber, M. E., M. A. Isaminger, C. Meuse, S. V. Vasiloff, and T. Shepherd, 1995: Comparative analysis of ground-based wind shear detection radars. *Proc. 1995 Int. Radar Conf.*, IEEE, Alexandria, VA, 486-495.

Weber, M. E., J. Y. N. Cho, J. S. Herd, J. M. Flavin, W. E. Benner, and G. S. Torok, 2007: The next-generation multimission U.S. surveillance radar network. *Bull. Amer. Meteor. Soc.*, **88**, 1739-1751.

Wilson, F. W., and R. H. Gramzow, 1991: The redesigned Low Level Wind Shear Alert System. Preprints, *4th Int. Conf. on Aviation Weather Systems*, Paris, France, 370.

Wolfson, M., D. Klingle-Wilson, M. Donovan, J. Cullen, D. Neilley, M. Liepins, R. Hallowell, J. DiStefano, D. Clark, M. Isaminger, P. Biron, and B. Forman, 1990: Characteristics of thunderstorm-generated low altitude wind shear: A survey based on nationwide Terminal Doppler Weather Radar testbed measurements. *Proc. 29th Conf. on Decision and Control*, IEEE, Honolulu, HI, 682-688.

Wolfson, M. M., R. L. Delanoy, B. E. Forman, R. G. Hallowell, M. L. Pawlak, and P. D. Smith, 1994: Automated microburst wind-shear prediction. *Linc. Lab. J.*, **7**, 399-426.

Zrnić, D. S., J. F. Kimpel, D. E. Forsyth, A. Shapiro, G. Crain, R. Ferek, J. Heimmer, W. Benner, T. J. McNellis, and R. J. Vogt, 2007: Agile-beam phased array radar for weather observations. *Bull. Amer. Meteor. Soc.*, **88**, 1753-1766.